Journal of
Materials in Life Sciences

Vol. 4 No. 2 (2025)

Full Paper

Hollow Silica-Encapsulated TiO_2 Functionalized with pH-Responsive Poly(acrylic acid) for Photocatalytic Degradation of Bisphenol A

Kiranraj Vadivellu[a], Elis Osman[a], Sheela Chandren[a,b]*

[a] Department of Chemistry, Faculty of Science, Universiti Teknologi Malaysia, 81310 UTM Johor Bahru, Johor, Malaysia.

[b] Centre for Sustainable Nanomaterials, Universiti Teknologi Malaysia, 81310 UTM Johor Bahru, Johor, Malaysia.

Article history
Received
15 October 2025
Revised
20 November 2025
Accepted
22 November 2025
Published online
31 November 2025

*Corresponding author
sheela@utm.my

Abstract

Titania (TiO_2) is widely recognized as a stable and non-toxic photocatalyst, yet its performance is restricted by a wide bandgap, rapid electron–hole recombination, and insensitivity to pH variations. Direct surface modification of TiO_2 with polymers further complicates applications, as the strong oxidative activity of TiO_2 can degrade organic components and compromise polymer stability. In this work, core–shell nanocomposites were engineered by encapsulating TiO_2 within hollow silica shells and subsequently modifying the outer surface with pH-responsive poly(acrylic acid) (PAA), forming PAA/SiO_2/*void*/TiO_2. The nanocomposites were synthesized using monomer volumes of 0.7, 1.4, and 2.1 mL, denoted as (0.7)PAA/SiO_2/*void*/TiO_2, (1.4)PAA/SiO_2/*void*/TiO_2, and (2.1)PAA/SiO_2/*void*/TiO_2, respectively. Structural and chemical analyses confirmed the successful integration of all components. ^{1}H NMR validated the PAA structure, while FTIR and TEM revealed characteristic bands and a distinct hollow core–shell morphology with uniform TiO_2 encapsulation and a stable SiO_2 framework, though the PAA layer was not visible due to its organic nature. UV–vis–NIR spectroscopy revealed a bandgap of 3.6 eV, attributed to the hybrid framework. Although substantially higher activity was expected with the addition of PAA, the degradation of bisphenol A (BPA) remained relatively low. The (0.7)PAA/SiO_2/*void*/TiO_2 achieved 16% degradation under UV and 7.5% under visible light, while higher PAA loadings further reduced activity due to excessive surface coverage. Despite the lower activity, the photocatalyst exhibited pH-responsive behavior, with BPA degradation increasing from 4.4% at pH 5 to 7.5% governed by the surface functionality of PAA. These findings highlight the potential of PAA/SiO_2/*void*/TiO_2 as pH-responsive photocatalysts for emerging contaminant degradation.

Keywords *titania, core-shell, photocatalysis, pH-responsive, bisphenol A*

1.0 INTRODUCTION

Titania (TiO_2), a versatile metal oxide semiconductor, has been extensively studied for its photocatalytic ability to degrade a wide range of environmental pollutants [1]. Among its polymorphs, anatase exhibits the highest photocatalytic activity due to its high surface area, superior charge carrier mobility, and lower electron–hole recombination rate [1, 2]. These properties, coupled with its stability, low toxicity, and affordability, make TiO_2 one of the most promising photocatalysts for environmental remediation and water treatment applications.

Despite its advantages, pristine TiO_2 faces critical limitations that restrict its performance. Its wide bandgap (E_g~3.2 eV) confines photoactivation to the ultraviolet (UV) region, which accounts for only a small fraction of solar energy [3]. Furthermore, rapid recombination of photoinduced charge carriers reduces photocatalytic efficiency, limiting its effectiveness under practical conditions [4]. Various modification strategies have been explored to overcome these drawbacks, such as doping with metals and non-metals or surface modification with polymers [5-7]. While these approaches can improve visible light response and charge separation, they often suffer from high cost, complicated synthesis, or stability issues.

Direct surface modification of TiO_2 with pH-responsive polymers, such as poly(acrylic acid) (PAA), offers certain advantages by introducing functional groups and improving dispersibility [8]. However, this strategy is not sustainable, as the strong oxidative activity of TiO_2 can degrade organic components, compromising polymer stability and long-term photocatalytic performance [9]. In order to overcome this limitation, TiO_2 can be encapsulated within hollow silica (SiO_2) shells, which act as protective barriers that prevent direct contact between TiO_2 and PAA (PAA/SiO_2/*void*/TiO_2 NCs). The SiO_2 shell provides structural stability, protects the PAA from degradation, and simultaneously preserves the intrinsic photocatalytic properties of TiO_2.

In addition to protection, hollow SiO_2 shells offer functional benefits. Their mesoporous structure allows pollutant molecules to diffuse through the SiO_2 layer and reach the encapsulated TiO_2 surface, ensuring photocatalytic activity is maintained [10]. At the same time, the hollow interior provides additional surface area and reactive sites, enhancing overall photocatalytic efficiency. Incorporating PAA onto the outer SiO_2 surface further introduces pH-responsive behavior, as the abundant carboxylic groups in PAA undergo protonation–deprotonation transitions depending on the solution pH [11]. This adaptive property enables modulation of surface charge and pollutant interactions, creating a responsive photocatalyst suitable for dynamic environmental conditions.

In this study, PAA/SiO_2/*void*/TiO_2 NCs were synthesized through a controlled process, where the monomer content was systematically varied to vary the polymer loading. The resulting photocatalysts were subjected to comprehensive characterization to confirm their structural integrity and physicochemical properties. Photocatalytic performance was then evaluated using bisphenol A (BPA) as a model pollutant under both UV and visible light irradiation. BPA, a widely used industrial chemical, frequently contaminates water systems through improper disposal and industrial discharge, and its persistence in the environment poses significant risks to ecosystems and human health [12]. These characteristics make BPA a priority target for photocatalytic degradation. Beyond photocatalytic activity, the pH-responsiveness of the PAA/SiO_2/*void*/TiO_2 NCs was also examined by assessing BPA degradation at different solution pHs.

2.0 MATERIALS AND METHOD

2.1 Materials

The following analytical-grade chemicals were used without any further purification: titanium(IV) oxide (TiO_2, ≥99.5%), 3-aminopropyltriethoxysilane (APS, 97%), methanol (99%), glucose (97%), ethanol (95% AR grade), 3-(2-aminoethylamino)propyltrimethoxysilane (AEAPS, 80%), tetraethyl orthosilicate (TEOS, 98%), aqueous ammonia (28%), acrylic acid (AA, 99%), 1,4-dioxane (99%), 4,4′-azobis(4-cyanovaleric acid) (ACVA, 98%), n-hexane, 4-cyano-4-(phenylcarbonothioylthio)pentanoic acid (CPADB), dimethylacetamide (DMAc, ≥99%), 4-dimethylaminopyridine (DMAP, ≥99%), N,N′-dicyclohexylcarbodiimide (DCC), and bisphenol A (BPA). Distilled water served as the primary solvent throughout all synthesis and washing procedures. All reagents were obtained from Aldrich unless otherwise specified.

2.2 Preparation of PAA/SiO_2/*void*/TiO_2 NCs

2.2.1 Preparation of SiO_2/*void*/TiO_2

The SiO_2/*void*/TiO_2 was prepared following the method proposed by Chandren and Ohtani [13]. Initially, TiO_2 (0.2 g) was dispersed in 10 mL of methanol containing APS (0.247 mL) and stirred vigorously at room temperature for 2 h. The suspension was centrifuged, washed with ethanol, and dried overnight at 80°C. The APS-modified TiO_2 (APS/TiO_2) was then treated with 65 mL of aqueous glucose solution (0.5 M), transferred into a 100 mL Teflon-lined autoclave, and heated at 180°C for 6 h to form a uniform polysaccharide coating. The resulting carbon-coated TiO_2 (C/TiO_2) was washed with ethanol and dried overnight at 80°C. Next, C/TiO_2 (0.2 g) was dispersed in 10 mL of methanol containing AEAPS (0.965 mL) and stirred for 2 h. The AEAPS-functionalized C/TiO_2 was then suspended in 10 mL of methanol containing TEOS (0.4273 mL), aqueous ammonia (0.5 mL), and distilled water (2 mL). The suspension was stirred for 1.5 h at room temperature to form a SiO_2 layer. The resulting SiO_2/C/TiO_2 was washed with ethanol, dried at 80°C, and finally calcined in air at 600°C for 2 h to remove the carbon layer, yielding SiO_2/*void*/TiO_2.

2.2.2 Preparation of PAA

PAA was synthesized via RAFT polymerization by varying the amount of acrylic acid monomer (0.7, 1.4, and 2.1 mL) which were selected in accordance with previous studies as they provide a suitable range of monomer concentrations that maintain good RAFT control while avoiding issues such as gelation or excessive viscosity at higher loadings [14, 15]. In a round-bottom flask equipped with a magnetic stirrer, 1,4-dioxane (5 mL) was mixed with acrylic acid, CPADB (0.1664 g), and ACVA (0.06 g). The solution was purged with nitrogen gas for 30 min, and stirred at 80°C for 24 h to initiate polymerization. The resulting polymer was precipitated with cold n-hexane (30 mL) and dried at room temperature for 24 h, yielding PAA. The different monomer volumes corresponded to low, medium, and high PAA concentrations, respectively, enabling a systematic evaluation of their effect on the final nanocomposites.

2.2.3 Esterification of PAA/SiO_2/*void*/TiO_2 NCs

The esterification of SiO_2/*void*/TiO_2 with PAA was carried out following the procedure reported by Anžlovar *et al.* [16]. Initially, PAA (0.3 g) was dissolved in DMAc (10 mL) to prepare the polymer solution. Next, SiO_2/*void*/TiO_2 (0.1 g) was dispersed into the solution under stirring to achieve uniform mixing. Once homogenized, DCC (0.295 g) and DMAP (0.175 g) were added as esterification catalysts. The mixture was stirred for 15 min, purged with nitrogen gas for 30 min, and maintained at 60°C under continuous stirring for 24 h to allow ester bond formation. After the reaction, the product was washed thoroughly with ethanol and dried at 50°C for 4 h. The resulting material was denoted as PAA/SiO_2/*void*/TiO_2 NCs. Sample codes corresponding to each synthesized composite are listed in Table 1.

Table 1: Coding of PAA/SiO_2/*void*/TiO_2 NCs prepared

Sample code	AA (mL)	TiO_2 (g)	Glucose concentration (M)	Silylation time (h)
(0.7)PAA/SiO_2/*void*/TiO_2 NCs	0.7	0.2	0.5	1.5
(1.4)PAA/SiO_2/*void*/TiO_2 NCs	1.4	0.2	0.5	1.5
(2.1)PAA/SiO_2/*void*/TiO_2 NCs	2.1	0.2	0.5	1.5

2.3 Characterization

PAA/SiO_2/*void*/TiO_2 NCs were characterized using a range of analytical techniques. The (0.7)PAA/SiO_2/*void*/TiO_2 NCs was selected for detailed characterization as a representative system, since all three variants exhibited qualitatively similar structural and optical features. Proton nuclear magnetic resonance (^{1}H NMR) spectroscopy was carried out on a Bruker DMX500 spectrometer operating at 400 MHz, with the polymer sample dissolved in deuterium oxide to confirm the polymer structure. Fourier-transform infrared (FTIR) spectroscopy was performed on a Perkin-Elmer Series 1600 spectrometer to identify functional groups, prepared by mixing the photocatalysts with potassium bromide (KBr) in a 1:100 ratio and scanning in the range of 400 – 4000 cm^{-1}. Transmission electron microscopy (TEM) was conducted on a high-resolution Hitachi HT7700 operated at 120 kV to examine the internal morphology and hollow core–shell structure of the composites. Optical absorption properties were determined using UV–vis–NIR spectroscopy on a JASCO V-670 spectrophotometer in the range of 200 – 800 nm, with the bandgap (E_g) estimated using the Tauc plot method.

2.4 Photocatalytic Testing

The photocatalytic activity of PAA/SiO_2/*void*/TiO_2 NCs was evaluated by monitoring the degradation of BPA under UV and visible light irradiation. A 6 W UV lamp was used as the UV source, while a Philips 18 W LED bulb served as the visible light source following the method reported by Lian *et al.* [17]. The experimental setup used for photocatalytic testing is shown in Figure 1. In each test, 50 mL of BPA solution (25 ppm) was mixed with 0.05 g of photocatalyst, and the suspension was stirred in the dark for 1 h to establish adsorption–desorption equilibrium. Following this step, the suspension was irradiated for 2 h, and 5 mL aliquots were withdrawn at specific intervals for analysis. BPA concentration was determined using a UV–Vis spectrophotometer, and the photocatalytic efficiency was calculated according to Equation 1.

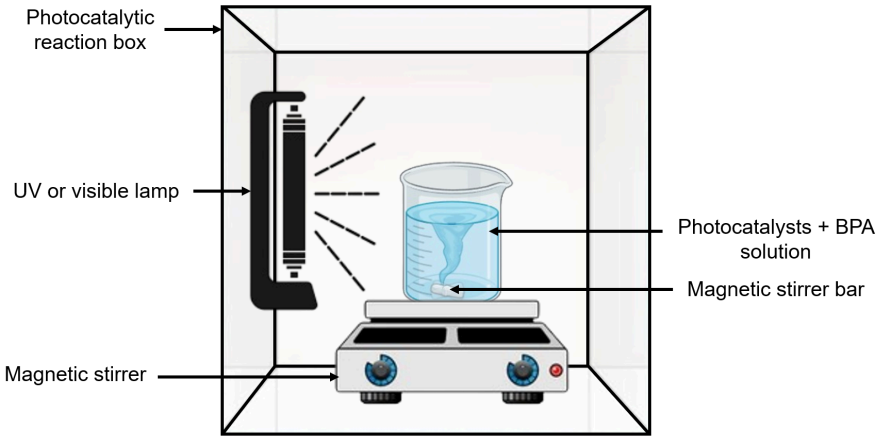

Figure 1 : Schematic illustration of the photocatalytic reaction setup

$$\text{Degradation percentage (\%)} = \frac{C_o - C}{C_o} \times 100\% \qquad \textbf{(Equation 1)}$$

Where C_o is the initial concentration after 1 h dark reaction, C is the concentration of BPA after being treated with UV and visible light irradiation.

2.5 pH-responsiveness Test

The pH-responsiveness of PAA/SiO_2/*void*/TiO_2 NCs was evaluated by assessing the photocatalytic degradation of BPA under visible light at pH 5, 7, and 9, representing acidic, neutral, and basic conditions. These values were selected to avoid extreme conditions that could compromise catalyst stability or alter degradation pathways, while still allowing the influence of pH on BPA solubility, ionization, and degradation efficiency to be examined. 50 mL of BPA (25 ppm) was adjusted to pH 5 with 0.05 M HCl, pH 9 with 0.05 M NaOH, while pH 7 remained unadjusted. Photocatalytic tests were carried out using the same procedure as the photocatalytic activity experiments, where photocatalysts were stirred in the dark for 1 h to establish adsorption–desorption equilibrium, followed by visible light irradiation with a Philips 18 W LED bulb for 2 h. After irradiation, 5 mL aliquots were withdrawn and analyzed using a UV–Vis spectrophotometer to determine BPA concentration, and degradation efficiency was calculated using Equation 1.

3.0 Results and Discussion

3.1 Physicochemical Properties of PAA/SiO_2/*void*/TiO_2 NCs

3.1.1 Structural Verification of PAA by ^{1}H NMR Spectroscopy

^{1}H NMR spectroscopy analysis was conducted to determine the chemical structure of PAA. Figure 2 shows the ^{1}H NMR spectra of acrylic acid (AA) and the synthesized PAA. The analysis focused exclusively on AA and PAA, as SiO_2 and TiO_2 are insoluble and lack NMR-active nuclei, rendering them unsuitable for this technique [18]. Figure 2(A) shows the spectrum of the AA, where characteristic vinylic proton peaks are observed at 5.8 ppm (a), 6.2 ppm (b), and 6.5 ppm (c), confirming the presence of –CH=CH_2 groups [19]. Detailed multiplet analysis of these signals reveals the expected scalar couplings for a vinyl AMX system. A trans-coupling between b and c of approximately $J_{b,c} \approx 16$ Hz, a cis-coupling between a and b of $J_{a,b} \approx 10$ Hz, and a geminal coupling between a and c of $J_{a,c} \approx 2$ Hz. These J-values are consistent with the stereoelectronic characteristics of the acrylic acid double bond. A sharp downfield signal at 12.4 ppm (d) corresponds to the carboxylic acid (–COOH) proton of AA [20].

In contrast, the ^{1}H NMR spectrum of PAA (Figure 2(B)) shows broad peaks at 1.6 ppm (a) and 2.2 ppm (b), assigned to methylene (–CH_2) and methine (–CH) protons along the polymer backbone. The signals in the 1.2 – 1.8 ppm correspond to –CH_2 groups [21], while those closer to 2.0 – 2.5 ppm are associated with –CH protons adjacent to –COOH groups [22]. The broad nature of these peaks reflects the high molecular weight and conformational flexibility of the polymer chains, which generate a distribution of chemical environments. Furthermore, the downfield –COOH signal typically observed between 10 – 13 ppm is absent, likely due to rapid proton exchange with D_2O and extensive hydrogen bonding, both of which suppress its detection [23]. The assigned chemical shifts and J-coupling constants for AA and PAA are summarized in Table 2.

Meanwhile, residual vinylic signals in the 5.8 – 6.5 ppm region indicate that some AA remained unreacted, suggesting incomplete polymerization, which may arise from insufficient reaction time, reduced initiator efficiency, or kinetic limitations during chain propagation [24]. Additional signals between 7 – 8 ppm were attributed to the aromatic protons of the RAFT agent (CPADB), confirming retention of the chain-end functionalities [25]. Hence, the emergence of broad PAA backbone signals, together with the RAFT end-group resonances, confirms the successful synthesis of PAA.

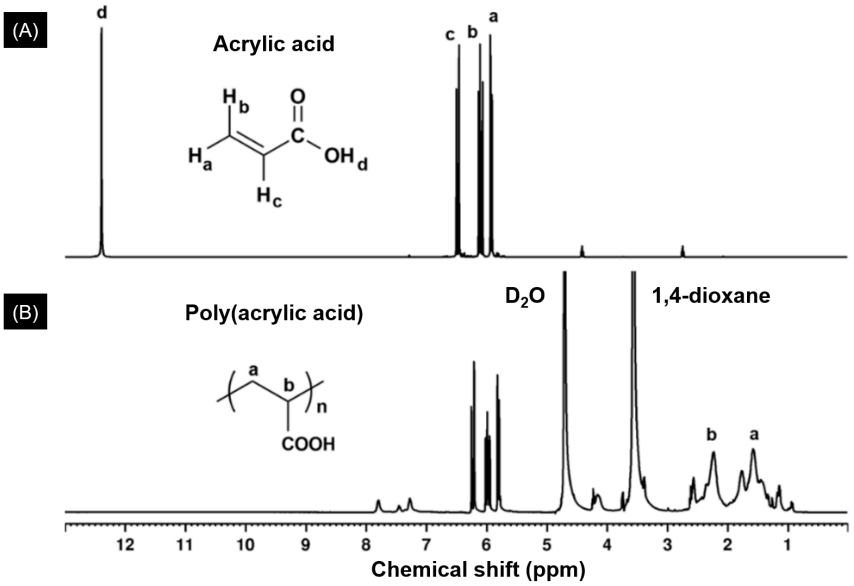

Figure 2 : ^{1}H NMR spectra of (A) Acrylic acid and (B) Poly(acrylic acid)

Table 2: Summary of ^{1}H NMR chemical shifts and J-couplings for AA and PAA

Sample	δ (ppm)	Proton	J (Hz)	Assignment
AA	5.80	a	$J_{a,b} \approx 10$; $J_{a,c} \approx 2$	Vinyl proton (–CH=$CH_{2)}$
	6.20	b	$J_{b,c} \approx 16$; $J_{a,b} \approx 10$	Vinyl proton (–CH=$CH_{2)}$
	6.45	c	$J_{b,c} \approx 16$; $J_{a,c} \approx 2$	Vinyl proton (–CH=$CH_{2)}$
	12.40	d	–	Carboxylic acid proton (–COOH)
PAA	1.6	a	–	–CH_2– backbone
	2.2	b	–	–CH– adjacent to –COOH

3.1.2 Functional Group Analysis by FTIR Spectroscopy

FTIR spectroscopy was employed to investigate the functional groups of the synthesized (0.7)PAA/SiO_2/*void*/TiO_2 NCs, with the corresponding spectrum presented in Figure 3. A broad absorption band centered at 3431 cm^{-1} is attributed to hydroxyl stretching (O–H) from carboxylic acid groups (–COOH) in PAA [26]. The broadness of this band indicates strong hydrogen bonding interactions, which may also involve surface O–H groups on TiO_2 or SiO_2 [27]. A weaker absorption near 3311 cm^{-1} is most likely due to N–H stretching vibrations originating from residual RAFT end-groups (CPADB) [28]. Distinct absorptions at 2926 and 2852 cm^{-1} correspond to aliphatic C–H stretching vibrations, consistent with the hydrocarbon backbone of PAA [26]. The band at 1627 cm^{-1} corresponds to C=O stretching, confirming the presence of COOH from PAA [29].

Moreover, a sharp absorption at 1092 cm^{-1} is assigned to Si–O stretching, indicating successful SiO_2 encapsulation [27]. Additional signals observed at 712, 672, 640, and 600 cm^{-1} are most likely due to Ti–O lattice vibrations characteristic of anatase TiO_2 [30]. Further peaks at 561, 522, and 455 cm^{-1} may be attributed to deeper Ti–O modes, suggesting a stable TiO_2 framework was retained even after encapsulation and surface modification. Therefore, these findings confirm that the PAA, SiO_2, and TiO_2 components were successfully integrated into the nanocomposites, while the fundamental structural integrity of TiO_2 was preserved.

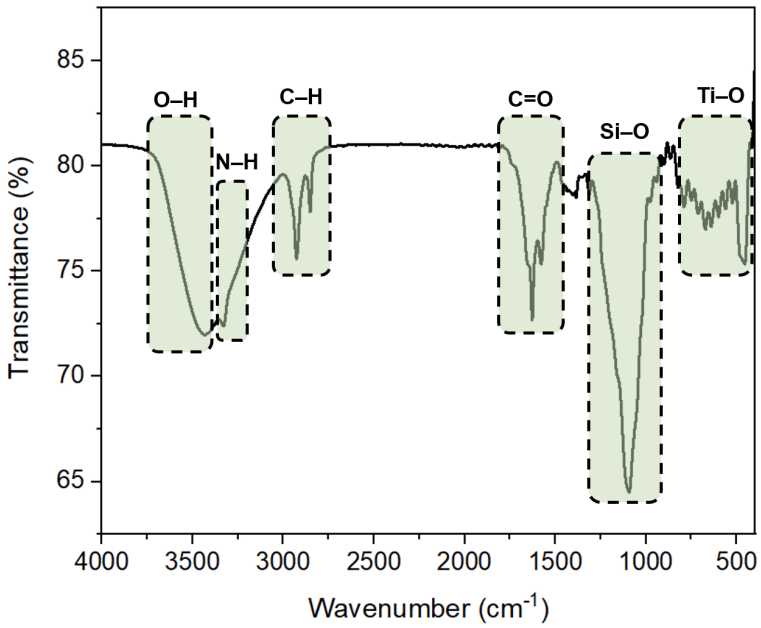

Figure 3 : FTIR spectrum of (0.7)PAA/SiO_2/*void*/TiO_2 NCs

3.1.3 Structural Properties by Transmission Electron Microscopy (TEM)

The structural properties of the (0.7)PAA/SiO_2/*void*/TiO_2 NCs are illustrated in Figure 4. The TEM image reveals a core–shell structure, where TiO_2 nanoparticles are encapsulated within an internal void and further surrounded by an outer SiO_2 layer. The central TiO_2 core, appearing as the darkest region due to its high electron density and strong scattering ability [31], has an average diameter of approximately 67 nm, consistent with previous studies reporting similar contrast features of TiO_2-based nanostructures [32]. This core serves as the photocatalytically active region, providing essential redox functionality.

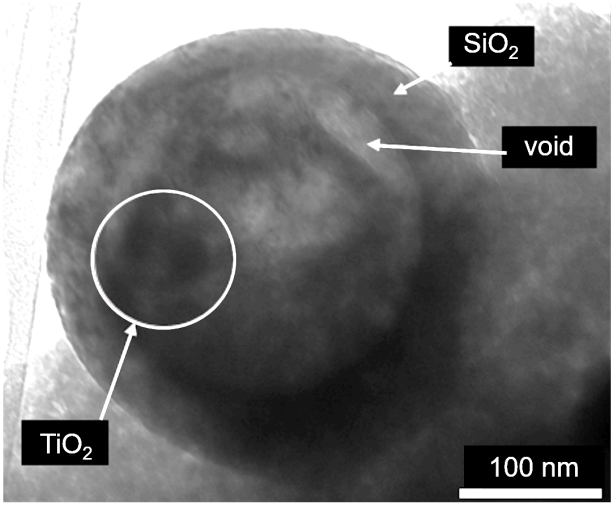

Figure 4 : TEM image of (0.7)PAA/SiO_2/*void*/TiO_2 NCs

Surrounding the TiO_2 is a lighter contrast void space, formed during the synthesis and subsequently defined by calcination. This void, with a measured thickness of around 119 nm, indicates the successful removal of the sacrificial carbon layer and contributes to lower particle density and enhanced molecular diffusion. In addition to the primary cavity, smaller low-density regions adjacent to the TiO_2 core can be observed, which may be attributed to localized dissolution or partial hollowing processes during heat treatment [33].

Encapsulating the entire structure is a SiO_2 shell, visible as a lighter grey boundary in the TEM image. This shell exhibits an average thickness of about 42 nm, most likely resulting from the controlled hydrolysis and condensation of TEOS

during silylation [34]. The shell plays a dual role: providing mechanical stability and chemical protection for the inner TiO_2 core, while also facilitating mass transport across the particle interface [35].

Although PAA is a crucial component in stabilizing and functionalizing the nanocomposites, it is not visible in TEM imaging due to its low electron density and organic nature, which produces negligible contrast under the electron beam [36]. Nonetheless, the TEM results confirm the successful fabrication of a hollow core–shell nanostructure comprising a TiO_2 core, an internal void, and an outer SiO_2 shell, validating the intended design of the (0.7)PAA/SiO_2/*void*/TiO_2 NCs.

3.1.4 Optical Properties and Bandgap Determination by Ultraviolet-visible-Near-Infrared (UV-vis-NIR) Spectroscopy

The optical properties of the (0.7)PAA/SiO_2/*void*/TiO_2 NCs were investigated using UV-vis-NIR absorption spectroscopy, as shown in Figure 5(a). The spectrum displays multiple absorption features arising from the organic and inorganic components of the nanocomposites. Two absorption peaks between 230 – 250 nm are attributed to electronic transitions in PAA [37]. Specifically, the peak near 230 nm corresponds to a $\pi \rightarrow \pi^*$ transition in the carbonyl group, while the weaker band around 250 nm is assigned to an $n \rightarrow \pi^*$ transition involving excitation of non-bonding electrons on oxygen atoms to the anti-bonding π^* orbital. These transitions confirm the presence of PAA functionalities in the nanocomposites.

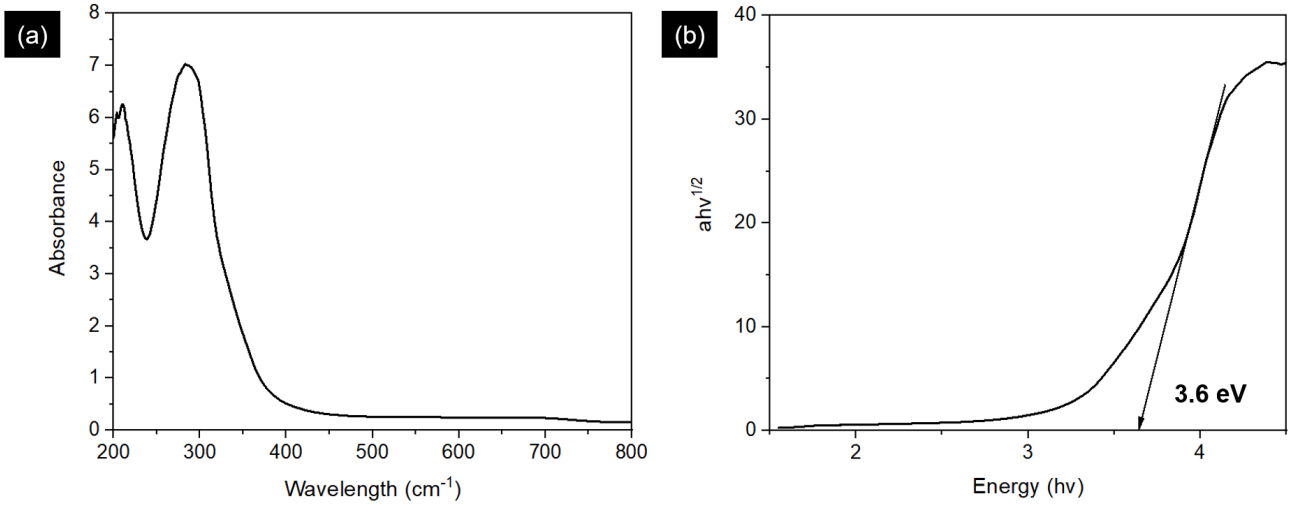

Figure 5 : (a) Absorption spectrum and (b) Tauc plot of the (0.7)PAA/SiO_2/*void*/TiO_2 NCs

A broader and more intense absorption band is observed between 290 and 310 nm, which corresponds to the fundamental band-to-band transition of anatase TiO_2 nanoparticles [38]. This transition arises from electron excitation from the O 2*p* valence band to the Ti 3*d* conduction band, a characteristic optical feature of TiO_2. The incorporation of SiO_2 may contribute to slight variations in peak intensity, but the dominant absorption features are consistent with those of PAA and TiO_2. Beyond 330 nm, the absorption intensity decreases sharply, with only weak tailing into the visible region, which may be attributed to scattering effects introduced by the hollow SiO_2 shell [39].

The E_g of the photocatalysts was evaluated using the Tauc plot approach. In this method, a plot of $(\alpha h\nu)^{1/2}$ against energy (hv) was constructed, and the E_g value was estimated by extrapolating the linear region of the curve to the x-axis. As shown in Figure 5(b), the linear extrapolation of the absorption edge yielded an E_g of 3.6 eV for the (0.7)PAA/SiO_2/*void*/TiO_2 NCs. This value is higher than the typical E_g of anatase TiO_2 (3.2 eV), indicating that the incorporation of the SiO_2 hollow shell and void structure significantly influences the optical properties of the system [40].

The increase in E_g can be attributed to dielectric confinement effects: the low dielectric constant of SiO_2 and the void space surrounding TiO_2 reduce charge screening, thereby increasing exciton binding energy and shifting the optical transition to higher energy [41]. Additionally, interfacial interactions between PAA functional groups and TiO_2 surfaces may further perturb the electronic band structure, contributing to the observed E_g widening [42].

Thus, these results confirm that the unique architecture of the nanocomposites modifies the local electronic environment of TiO_2, resulting in a widened E_g and altered optical behaviour compared to bare TiO_2. Such modifications may influence charge separation and photocatalytic activity, highlighting the importance of structural design in tailoring semiconductor–polymer composites for environmental applications.

3.2 Photocatalytic Testing

The photocatalytic activity of the synthesized PAA/SiO_2/*void*/TiO_2 NCs under UV irradiation was conducted using BPA as a model contaminant, and the results are presented in Figure 6. After 2 h of exposure, distinct differences in degradation efficiencies were observed, demonstrating the strong influence of material composition on photocatalytic performance. The commercial TiO_2 exhibited the highest activity, achieving 91.1% degradation of BPA. This high efficiency is consistent with the well-known photocatalytic behaviour of TiO_2, attributed to its suitable E_g for UV absorption, high surface area, and effective charge separation [43]. In contrast, the photolysis control, performed without any photocatalyst, resulted in only 13% degradation, confirming that BPA is relatively stable under UV light alone and that the presence of a photocatalyst is essential for efficient degradation [44].

Although it was hypothesized that the addition of PAA would significantly enhance BPA degradation by improving the interaction between the photocatalysts and the surrounding medium, the experimental results did not reflect the same. The (0.7)PAA/SiO_2/*void*/TiO_2 NCs achieved the highest BPA removal efficiency of 16%, slightly above photolysis alone, whereas the (1.4)PAA/SiO_2/*void*/TiO_2 NCs and (2.1)PAA/SiO_2/*void*/TiO_2 NCs exhibited lower efficiencies of 5% and 2%, respectively. The decline in photocatalytic performance with higher PAA loadings is likely due to the formation of thicker polymer layers or longer polymer chains that hinder light penetration, reduce the number of exposed TiO_2 active sites, and limit charge carrier transport [45]. Nevertheless, the inclusion of PAA was intended to impart pH-responsive functionality and determine how variations in solution pH influence the photocatalytic behaviour of the nanocomposites.

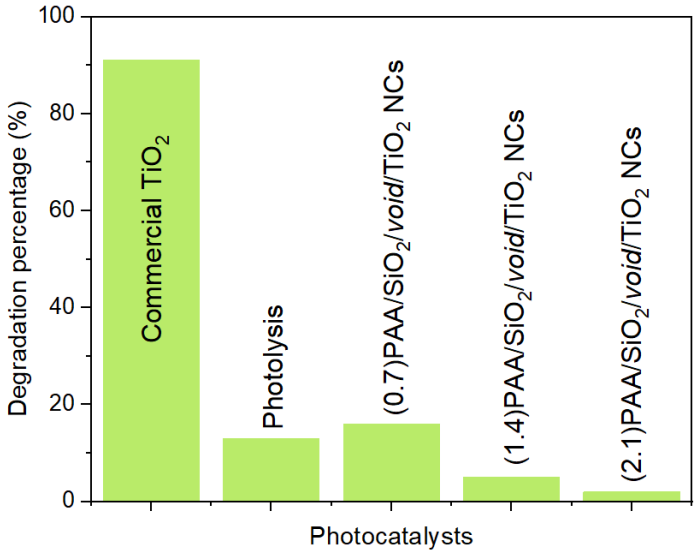

Figure 6 : Degradation efficacy of BPA under UV light irradiation in the presence of different photocatalysts. Experiment condition: addition of photocatalyst (0.05 g) in BPA (25 ppm) and reaction time of 2 h

Since UV light represents only a minor portion of the solar spectrum, achieving photocatalytic activity under visible light is crucial for practical applications in pollutant degradation. For this reason, the best-performing photocatalysts under UV irradiation (0.7)PAA/SiO_2/*void*/TiO_2 NCs were evaluated alongside commercial TiO_2 under visible light exposure. The results, shown in Figure 7, reveal that commercial TiO_2 achieved 9% BPA degradation after 2 h, while the (0.7)PAA/SiO_2/*void*/TiO_2 NCs displayed a slightly lower degradation efficiency of 7.5%. The limited activity observed for both materials arises from the wide E_g of TiO_2, which restricts absorption primarily to the UV region, thereby suppressing efficient charge carrier generation under visible light [43]. In addition, the PAA coating in the nanocomposites may have further hindered photon absorption and charge transfer, slightly reducing photocatalytic efficiency compared to commercial TiO_2 [6].

These results emphasize that although (0.7)PAA/SiO_2/*void*/TiO_2 NCs perform relatively well under UV light, their photocatalytic activity does not extend effectively into the visible range. This limitation highlights the need for further material modifications, particularly to improve responsiveness under visible light irradiation. In addition to light responsiveness, photocatalytic efficiency is also strongly governed by the solution environment, where pH can alter surface charge properties and pollutant speciation. Therefore, the next investigation examines how varying pH conditions influence the photocatalytic performance of the nanocomposites.

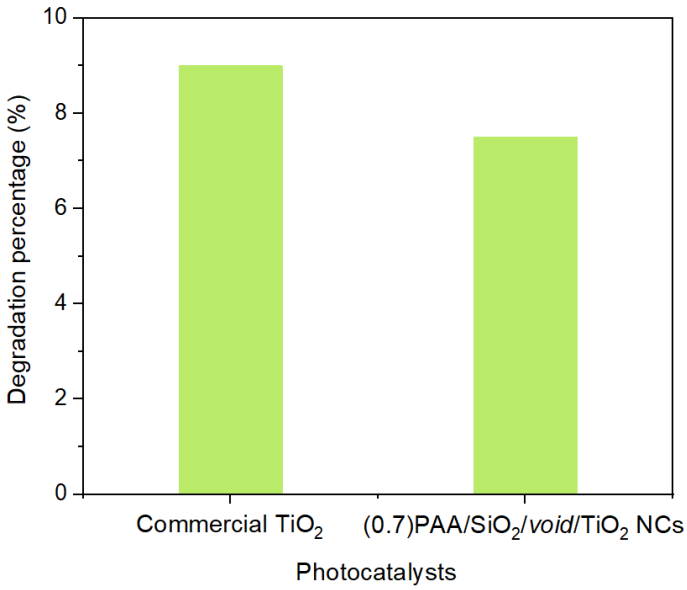

Figure 7 : Degradation efficacy of BPA under visible light exposure utilizing commercial TiO_2 and (0.7)PAA/SiO_2/*void*/TiO_2 NCs. Experiment condition: addition of photocatalyst (0.05 g) in BPA (25 ppm) and reaction time of 2 h

3.3 pH-responsiveness Test

The pH-responsiveness of the synthesized (0.7)PAA/SiO_2/*void*/TiO_2 NCs was evaluated by examining their photocatalytic degradation of BPA under visible light irradiation. This assessment provides insight into how acidic, neutral, and basic environments influence photocatalytic activity, reflecting both the stability and adaptability of the photocatalysts. BPA solutions were adjusted to pH 5, 7, and 9 to represent conditions relevant to practical aqueous systems.

As shown in Figure 8, the degradation efficiencies at pH 5, 7, and 9 were 4.4%, 6.0%, and 7.5%, respectively. These results indicate a modest but consistent improvement in photocatalytic activity as the solution shifts from acidic toward alkaline conditions. Under acidic conditions (pH 5), the photocatalyst surface is likely protonated, which reduces electrostatic interaction with BPA molecules and limits the generation of reactive species such as hydroxyl radicals [46]. In contrast, at pH 7 and 9, the photocatalyst surface becomes increasingly negatively charged, enhancing electrostatic attraction with deprotonated BPA molecules and facilitating the formation of hydroxyl radicals from available hydroxide ions [47]. This progression accounts for the higher degradation efficiency observed under alkaline conditions.

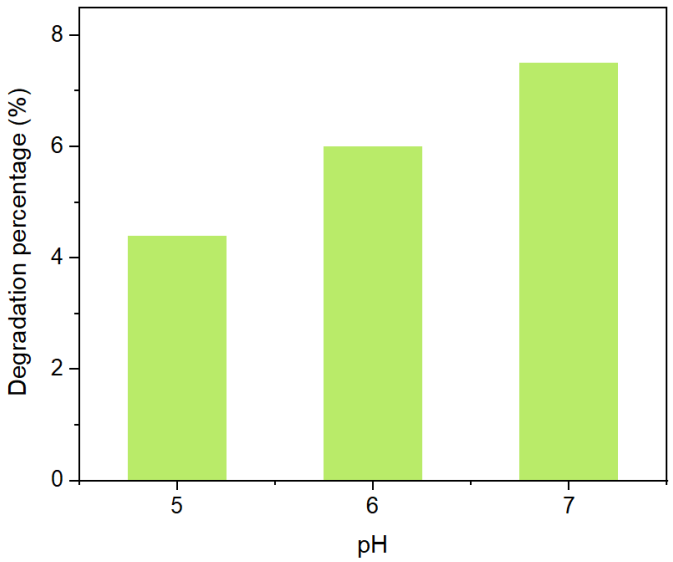

Figure 8 : Degradation efficacy of BPA under visible light irradiation in the presence of (0.7)PAA/SiO_2/*void*/TiO_2 NCs with different pH. Experiment condition: photocatalyst (0.05 g) was added to BPA with different pHs and a reaction time of 2 h

The influence of pH is further clarified by the conformational behaviour of the PAA chains in the nanocomposites, as shown in Figure 9. At low pH, the COO^- of PAA is protonated, resulting in neutralized chains that collapse toward the TiO_2 surface. This compact conformation forms a dense barrier, hindering the diffusion of BPA molecules and light to the catalytic core, thereby suppressing photodegradation efficiency [48]. In contrast, at higher pH, deprotonation of COOH introduces electrostatic repulsion among polymer chains, causing them to swell and expand [49]. This swollen state increases the contact surface and facilitates the diffusion of pollutants and photons towards TiO_2, thus enhancing photocatalytic activity.

Despite the slight enhancement at higher pH, the overall degradation percentages remained low, indicating that the current nanocomposite structure is not sufficiently effective under visible light. This limitation likely arises from restricted light absorption and rapid recombination of photogenerated charge carriers, which reduces the formation of reactive species. Nonetheless, the results confirm that the (0.7)PAA/SiO_2/*void*/TiO_2 NCs exhibit measurable pH responsiveness, suggesting that further structural modifications, such as the incorporation of visible-light-active dopants, could significantly improve photocatalytic performance across different environmental conditions.

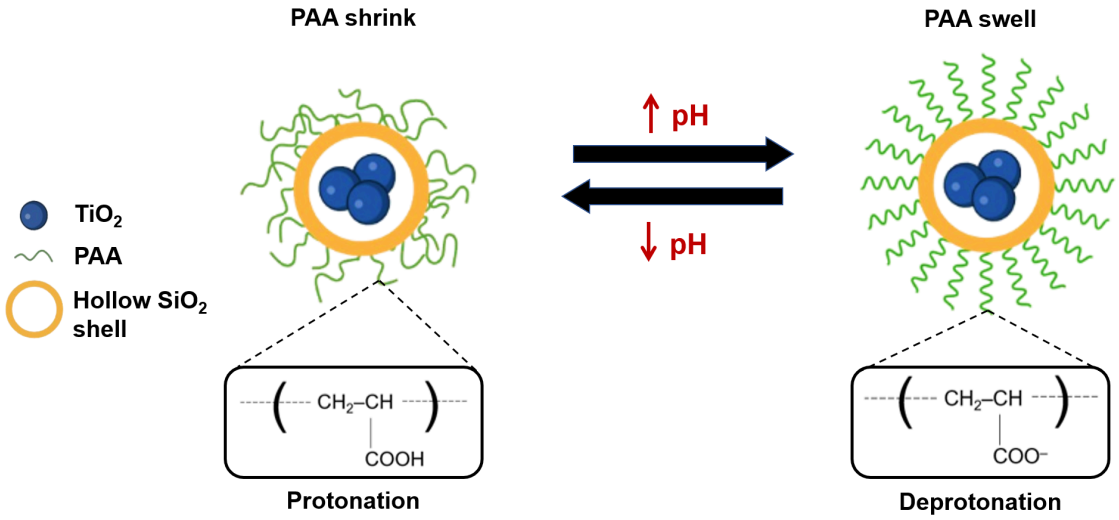

Figure 9 : Illustration of (0.7)PAA/SiO_2/*void*/TiO_2 NCs behaviour under different pH

4.0 CONCLUSION

This study successfully synthesized PAA/SiO_2/*void*/TiO_2 NCs with varying PAA loadings via controlled encapsulation and polymer functionalization. Characterization confirmed the formation of hollow core–shell structures with retained anatase crystallinity. Optical analysis indicated a widened E_g (3.6 eV) due to the SiO_2 shell and PAA interactions. Photocatalytic testing showed that the (0.7)PAA/SiO_2/*void*/TiO_2 NCs achieved only 16% degradation of BPA under UV light, while higher PAA loadings further reduced activity due to excessive surface coverage and hindered charge transport. Under visible light, both the (0.7)PAA/SiO_2/*void*/TiO_2 NCs and commercial TiO_2 displayed limited photocatalytic activity, reflecting the wide E_g of TiO_2 and restricted photoresponse in this region. Although the overall photocatalytic efficiencies were low, the incorporation of PAA introduced pH-responsive behaviour, with enhanced photocatalytic performance under alkaline conditions attributed to polymer chain swelling that improved substrate diffusion and surface interactions. These findings demonstrate that PAA/SiO_2/*void*/TiO_2 NCs provide a tunable, pH-responsive platform for photocatalytic applications, offering opportunities for further modification to improve visible-light-driven degradation of organic pollutants.

Acknowledgement

The authors would like to acknowledge funding provided by Universiti Teknologi Malaysia from Geran Penyelidikan Hi-Tech (F4) (Q.J130000.4654.00Q19) and PDRU Grant Vote No. 07E44.

References

[1] Chauke, N. M., Ngqalakwezi, A., & Raphulu, M. (2025). Transformative advancements in visible-light-activated titanium dioxide for industrial wastewater remediation. *International Journal of Environmental Science and Technology*, 22(9), 8521–8552.

[2] Hossain, R., Hollow, J., Chesterfield, V., Langley, D., & Apblett, A. (2025). Design, synthesis, and structural characterization of Fe^{2+}-doped anatase TiO_2 nanocrystals and its impact on electronic properties and photocatalytic activity. *Materials Advances*, 21: 7821-7836.
[3] Madima, N., Chauke, N. M., Ngqoloda, S., Mmelesi, O. K., & Raphulu, M. (2025). Recent advances in the development of defective black TiO_2 nanomaterials for application in energy and environmental sustainability: A review. *Results in Engineering*, 26, 104868.
[4] Paiu, M., Lutic, D., Favier, L., & Gavrilescu, M. (2025). Heterogeneous photocatalysis for advanced water treatment: Materials, mechanisms, reactor configurations, and emerging applications. *Applied Sciences*, 15, 5681.
[5] Manoj, G. M., Shalini, M., Thenmozhi, K., Ponnusamy, V. K., & Hari, S. (2024). Recent advancements in the surface modification and functionalization of magnetic nanomaterials. *Applied Surface Science Advances*, 21, 100608.
[6] Zango, Z. U., Ibnaouf, K. H., Garba, A., Aldaghri, O., Wadi, I. A., Hosseini-Bandegharaei, A., & Baigenzhenov, O. (2025). Advances in green synthesis, modification strategies, and photocatalytic application of metal oxide nanoparticles for organic pollutants degradation: A comprehensive and in-depth review. *Journal of Molecular Liquids*, 428, 127497.
[7] Dostanić, J., Lončarević, D., Hadnađev-Kostić, M., & Vulić, T. (2024). Recent advances in the strategies for developing and modifying photocatalytic materials for wastewater treatment. *Processes*, 12, 1914.
[8] Hajareh Haghighi, F., Mercurio, M., Cerra, S., Salamone, T. A., Bianymotlagh, R., Palocci, C., Romano Spica, V., & Fratoddi, I. (2023). Surface modification of TiO_2 nanoparticles with organic molecules and their biological applications. *Journal of Materials Chemistry B*, 11(11), 2334–2366.
[9] El Mchaouri, M., Mallah, S., Abouhajjoub, D., Boumya, W., Elmoubarki, R., Essadki, A., Barka, N., & Elhalil, A. (2025). Engineering TiO_2 photocatalysts for enhanced visible-light activity in wastewater treatment applications. *Tetrahedron Green Chemistry*, 6, 100084.
[10] Xiao, N., Zhang, A. A., Yuan, K., & Cao, W. (2025). Robust mesoporous SiO_2-coated TiO_2 colloidal nanocrystal with enhanced adsorption, stability, and adhesion for photocatalytic antibacterial and benzene removal. *Materials*, 18, 3844.
[11] Zhu, X., Liu, W., AlMasoud, N., Alomar, T. S., Sun, J., Fu, C., & Zhou, J. (2024). Temperature and pH dual dependent conformational transition of polyacrylic acid modified by dehydroabietic alcohol. *Advanced Composites and Hybrid Materials, 8*(1), 80.
[12] Kurre, D., & Samantaray, S. (2025). Sources and causes of emerging contaminants. In M. K. Jindal, P. Baranwal, & B. Das (Eds.), *Emerging Contaminants in Water* (pp. 49–88). Cham: Springer Nature Switzerland.
[13] Chandren, S., & Ohtani, B. (2012). Preparation, characterization and photocatalytic performance of titania particles encapsulated in hollow silica shells as an efficient photocatalyst for redox-combined stereoselective synthesis of L-pipecolinic acid from L-lysine. *Journal of Photochemistry and Photobiology A: Chemistry, 246,* 50–59.
[14] Alshammari, K. (2024). Influence of ZrO_2 nanoparticles on the structural and photocatalytic properties of three-dimensional PVA/g-C_3N_4 polymer films. *Journal of Alloys and Compounds, 1003,* 175622.
[15] Freitas, A. G. O., Muraro, P. I. R., Bortolotto, T., Trindade, S. G., Schmidt, V., Lopes, L. Q. S., Ninago, M., Satti, A., Ciolino, A., Villar, M., & Giacomelli, C. (2019). Facile one-pot synthesis and solution behavior of poly(acrylic acid)-block-polycaprolactone copolymers. *Journal of Molecular Liquids, 273,* 99–106.
[16] Anzlovar, A., Huskić, M., & Žagar, E. (2016). Modification of nanocrystalline cellulose for application as a reinforcing nanofiller in PMMA composites. *Cellulose, 23,* 505–518.
[17] Lian, F., Batool, F., Anjum, M., Qadeer, S., Idris, A. M., Nisa, W., Rao, Z., & Ullah, H. (2025). Transforming apricot kernel shell into a multifunctional photocatalyst for wastewater treatment and antimicrobial applications. *Frontiers in Environmental Science, 13,* 1547291.
[18] Mitschke, N., Vemulapalli, S. P. B., & Dittmar, T. (2023). NMR spectroscopy of dissolved organic matter: A review. *Environmental Chemistry Letters, 21*(2), 689–723.
[19] Gao, X., Wang, X., Yu, J., Ding, B., & Zhang, X. (2025). Synthesis of poly(acrylonitrile-co-acrylic acid) for high-strength carbon nanofibers. *ACS Applied Polymer Materials, 7*(6), 4002–4008.
[20] Gerothanassis, I., & Kupka, T. (2025). New insights into nuclear magnetic resonance (NMR) spectroscopy. *Molecules, 30,* 1–25.
[21] Sözügeçer, S., & Bayramgil, N. P. (2021). Preparation and characterization of polyacrylic acid-hydroxyapatite nanocomposite by microwave-assisted synthesis method. *Heliyon, 7*(6), e07226.
[22] Venianakis, T., Primikyri, A., Alexandri, E., Papamokos, G., & Gerothanassis, I. P. (2021). Molecular models of three ω-3 fatty acids based on NMR and DFT calculations of ^{1}H NMR chemical shifts. *Journal of Molecular Liquids, 342,* 117460.
[23] Fontana, C., & Widmalm, G. (2023). Primary structure of glycans by NMR spectroscopy. *Chemical Reviews, 123*(3), 1040–1102.
[24] Jackson, N. E., & Savoie, B. M. (2025). Ten problems in polymer reactivity prediction. *Macromolecules, 58*(4), 1737–1754.
[25] Yu, C., Ha, J., Park, M., Lee, J., Choi, J., Park, B. Y., Boyer, C., Min, S. K., & Kwon, M. S. (2025). Rapid and precise synthesis of acrylic polymers driven by visible light. *Chemical Science, 16*(25), 11626–11636.
[26] Muñoz-García, R. O., Ruiz-Casillas, C. A., Lomelí-Rosales, D. A., Cortés-Ortega, J. A., Sánchez-Díaz, J. C., & Cruz-Barba, L. E. (2025). A poly(acrylic acid)-based hydrogel crosslinked with hydroxypropylcellulose as a clarifying agent in nickel(II) solutions. *Gels, 11,* 560.
[27] Armendáriz-Alonso, E. F., Rivera-García, N., Moreno-Razo, J. A., Meza-Espinoza, L. O., Waldo-Mendoza, M. A., & Pérez, E. (2025). Structural water content in pigment-grade TiO_2 particles coated with Al_2O_3 and SiO_2, and their effect on polypropylene photodegradation. *Coatings, 15,* 685.
[28] Darmayanti, M. G., Tuck, K. L., & Thang, S. H. (2025). κ-Carrageenan-grafting-copolymers by RAFT polymerization exhibiting CO_2 adsorption properties. *Carbohydrate Polymer Technologies and Applications, 11,* 100995.

[29] Sarafraz, O., Bamoniri, A., Mirjalili, B. B. F., & Moghaddam, R. H. (2025). Uranium removal from water samples by a new adsorbent based on amino acid grafted biopolymer/polyacrylic acid using a high energy irradiation method. *Journal of Polymers and the Environment, 33*(9), 4162–4179.
[30] Roškarič, M., Žerjav, G., Zavašnik, J., Finšgar, M., & Pintar, A. (2025). Effect of TiO_2 morphology on the properties and photocatalytic activity of g-C_3N_4/TiO_2 nanocomposites under visible-light illumination. *Molecules, 30,* 460.
[31] Gong, T., Chen, L., Wang, X., Qiu, Y., Liu, H., Yang, Z., & Walther, T. (2025). Recent developments in transmission electron microscopy for crystallographic characterization of strained semiconductor heterostructures. *Crystals, 15*(2), Article 192.
[32] Sellami, H., Akinyemi, M. O., Gdoura-Ben Amor, M., Onwudiwe, D. C., & Mthiyane, D. M. N. (2025). Structural and optical characterization of TiO_2 nanoparticles synthesized using *Globularia alypum* leaf extract and the antibacterial properties. *Discover Applied Sciences, 7*(8), 834.
[33] Stopic, S., Kostić, D., Emil-Kaya, E., Uysal, E., Gürmen, S., Mitrašinović, A., Perušić, M., & Friedrich, B. (2024). High-pressure and high-temperature dissolution of titanium from titanium and aluminum residues: A comparative study. *Surfaces, 7*(4), 1096–1108.
[34] Crucho, C. I. C. (2024). Silica coatings: From nanostructures to biological entities. *Applied Materials Today, 38*, 102179.
[35] Yu, H., & Xie, J. (2025). Core–shell microcrystalline cellulose and rutile nano-titanium dioxide composite for sunscreen: Synthesis and broad-spectrum UV protection mechanism. *Industrial Crops and Products, 235*, 121833.
[36] Biran, I., Houben, L., Kossoy, A., & Rybtchinski, B. (2024). Transmission electron microscopy methodology to analyze polymer structure with submolecular resolution. *The Journal of Physical Chemistry C, 128*(14), 5988–5995.
[37] Burresi, E., Protopapa, M. L., Yao, L., & Yang, H. (2024). Optical investigation of degradation of graphene oxide in an alkaline environment: Evidence of two distinct photon-emitting phases in the visible region. *Carbon Trends, 17*, 100412.
[38] Zhou, H., Wang, H., Yue, C., He, L., Li, H., Zhang, H., Yang, S., & Ma, T. (2024). Photocatalytic degradation by TiO_2–conjugated/coordination polymer heterojunction: Preparation, mechanisms, and prospects. *Applied Catalysis B: Environment and Energy, 344*, 123605.
[39] Polché, M. A.-O., José Miguel, B. F., Guzmán González, C. A., González Contreras, G. A.-O. X., & Romero Arellano, V. H. A.-O. (2023). Study of the scattering effect by SiO_2 nanoparticles, in a luminescent solar concentrator sensitized with carbon dots. *Nanomaterials, 13*(1), 2079–4991.
[40] Taha, M., Ghalia, A., Farid, A., Abdallah, S., & Soliman, T. (2024). Controlling the shell thickness of SiO_2 on TiO_2 NPs: Characterization, linear and nonlinear optical properties. *Ceramics International, 50*(1), 1401–1413.
[41] Forde, A., Tretiak, S., & Neukirch, A. J. (2023). Dielectric screening and charge-transfer in 2D lead-halide perovskites for reduced exciton binding energies. *Nano Letters, 23*(1), 1530–6992.
[42] Zhu, X., He, J., Zhang, R., Cong, C., Zheng, Y., Zhang, H., Zhang, S., & Chen, L. (2020). Effects of dielectric screening on the excitonic and critical points properties of WS_2/MoS_2 heterostructures. *Nanoscale, 12*(46), 23732–23739.
[43] He, X., Fang, H., Gosztola, D. J., Jiang, Z., Jena, P., & Wang, W.-N. (2019). Mechanistic insight into photocatalytic pathways of MIL-100(Fe)/TiO_2 composites. *ACS Applied Materials & Interfaces, 11*(13), 12516–12524.
[44] Ghosh, S., Pourebrahimi, S., Malloum, A., Ajala, O. J., AlKafaas, S. S., Onyeaka, H., Nnaji, N. D., Oroke, A., Bornman, C., Christian, O., Ahmadi, S., & Wani, M. Y. (2023). A review on ciprofloxacin removal from wastewater as a pharmaceutical contaminant: Covering adsorption to advanced oxidation processes to computational studies. *Materials Today Communications, 37*, 107500.
[45] Gangan, A., Fahmy, A., Shaban, S. A., & El-Bahy, Z. M. (2025). Plasma modification of the structural, morphological, and catalytic activity of Fe_3O_4@SiO_2@TiO_2 core–shell system. *Advanced Composites and Hybrid Materials, 8*(2), 178.
[46] Yuan, Q., Xiao, L., Gao, S., Abdukayum, A., Kong, Q., Hu, G., Dubal, D., & Zhou, Y. (2025). From fundamentals to mechanisms: Peroxyacetic acid catalysts in emerging pollutant degradation. *Materials Today, 87*, 197–230.
[47] Bissenova, M., Idrissov, N., Kuspanov, Z., Umirzakov, A., & Daulbayev, C. (2025). Hybrid adsorption–photocatalysis composites: A sustainable route for efficient water purification. *Materials for Renewable and Sustainable Energy, 14*(2), 44.
[48] Hunge, Y. M., Yadav, A. A., Khan, S., Takagi, K., Suzuki, N., Teshima, K., Terashima, C., & Fujishima, A. (2021). Photocatalytic degradation of bisphenol A using titanium dioxide@nanodiamond composites under UV light illumination. *Journal of Colloid and Interface Science, 582*, 1058–1066.
[49] Philip, A. K., Samuel, B. A., Saleh, Y. S., Bhatia, S., Mohammad, B. I., & Al-Aubaidy, H. A. (2025). pH-responsive agarose hydrogel for enhanced gastrointestinal ibuprofen delivery: A novel pressure-sensitive adhesive system. *Next Materials, 8*, 100790.